RSC Advances

PAPER

View Article Online
View Journal | View Issue

Cite this: *RSC Adv.*, 2026, **16**, 9085

Synthesis of siloxane-integrated Schiff base compounds exhibiting aggregation-induced emission properties

Yuling Li,[a] Depeng Ma,[b] Fanzhen Kong,[c] Yuanrong Wang,[d] Lianfeng Wu,[ef] Zhihui Yang[fgh] and Haifeng Lu*[fgh]

Received 26th December 2025
Accepted 3rd February 2026

DOI: 10.1039/d5ra10030e

rsc.li/rsc-advances

Schiff base compounds have garnered considerable research interest due to their promising fluorescence properties. In this work, we successfully synthesized two Schiff base compounds as aggregation-induced emission (AIE)-active luminescent agents using a simple and efficient one-step method. The molecular design of these compounds effectively combines the dual advantages of Schiff base structures and AIE effects, retaining the chemical stability and tunable optical properties of Schiff base compounds while exhibiting the unique AIE property of significantly enhanced fluorescence in the aggregated state. Owing to these AIE characteristics, the synthesized compounds show potential for application in biomedicine, including bioimaging, fluorescence sensing, and information security.

Introduction

Schiff bases are defined as compounds containing imine or methylimine groups (–RC═N–), and are typically formed *via* the condensation of primary amines with reactive carbonyl groups.[1] Due to their ease of synthesis, strong coordination ability, and favorable fluorescence properties,[2–5] Schiff bases have attracted considerable research attention over recent decades. However, while most studies on Schiff bases predominantly focus on their use as fluorescence sensors,[6,7] relatively few have examined their inherent fluorescence properties and structure–activity relationships.[8]

Conventional fluorescent molecules often undergo aggregation-caused quenching (ACQ), a phenomenon where fluorescence diminishes at high concentrations or in the aggregated state due to π–π stacking interactions that promote the formation of quenching species, such as excimers.[9] This limits their utility in applications requiring aggregated forms, such as solid films for optoelectronic devices and concentrated fluorescent probes. In contrast, aggregation-induced emission (AIE) compounds exhibit enhanced fluorescence in the aggregated state, thereby overcoming ACQ and offering promise for practical applications.[10–14] AIE materials have recently attracted attention for their utility in optoelectronics and biomedical imaging, alongside their potential for use as biosensors. Their advantages—including deep tissue penetration ability,[15,16] minimal autofluorescence, high photostability, and low biotoxicity[17]—render them suitable for analytical detection, multimodal bioimaging, light-controlled drug release, and photodynamic therapy.[18–20] Therefore, synthesizing Schiff base compounds with AIE properties is critical for producing photostable probes that overcome the limitations of traditional ACQ fluorophores.

Studies on AIE have achieved success through the development of nanoplatforms that employ AIE compounds as photosensitizers.[21–23] For example, Liu *et al.*[24] prepared luminescent nanoparticles from tetraphene derivatives with strong AIE properties; by combining these with the triplet sensitizer platinum octaethylporphyrin (PtOEP), they achieved aggregation-induced photon upconversion (iPUC). Additionally, a multifunctional nanoplatform, TUT NPs, was developed using AIE-active photosensitizers, MXene Ti_3C_2 nanosheets, and UCNPs,[25] yielding intense near-infrared fluorescence under 808 nm excitation through the combined action of the individual components. Unlike these complex methodologies, we focus here on a streamlined molecular design strategy. We report a straightforward, one-step synthesis of two novel siloxane-integrated Schiff base compounds, PBS and OBS. The deliberate incorporation of a flexible siloxane spacer aims to suppress detrimental π–π stacking and enhance AIE,[26–29] while

[a]*School of Engineering Science, Shandong Xiehe University, Jinan, 250109, P. R. China*
[b]*School of Radiology, Shandong First Medical University, Shandong Academy of Medical Sciences, Taian, Shandong Province, 271016, P. R. China*
[c]*SICO Performance Material (Shandong) Co., Ltd, Jining New Materials Industrial Park, Jining, Shandong Province, 272200, P. R. China*
[d]*Chambroad Chemical Industry Research Institute Co., Ltd, Binzhou, Shandong Province, 251700, P. R. China*
[e]*Marine Chemical Research Institute Co. Ltd, Qingdao, Shandong Province, 266071, P. R. China*
[f]*State Key Laboratory of Coatings for Advanced Equipment, 266071, P. R. China*
[g]*Key Laboratory of Special Functional Aggregated Materials (Shandong University), Ministry of Education, China*
[h]*School of Chemistry and Chemical Engineering, Shandong University, Jinan 250100, P. R. China*

the Schiff base core offers a facile site for structural tuning and metal ion coordination.[30,31]

In this study, two siloxane-containing Schiff base compounds, PBS and OBS, were synthesized from MM^{NH_2} and *p*-hydroxybenzaldehyde or *o*-hydroxybenzaldehyde, respectively (Scheme 1), in which (a) represents PBS and (b) represents OBS, and their luminescence properties were subsequently investigated. The strong solid-state emission of PBS suggests utility in developing "turn-on" fluorescent sensors for solid-phase or high-viscosity environments, such as test strips for on-site detection of analytes or probes for monitoring polymerization processes where conventional dyes quench. Furthermore, the combination of AIE-driven brightness, enhanced photostability, and the potential biocompatibility conferred by the siloxane moiety positions these compounds as promising candidates for long-term, high-fidelity bioimaging, addressing the critical limitation of photobleaching in conventional fluorescent tags [32–35]. The comparative study of the *para-* (PBS) and *ortho-*substituted (OBS) analogues provides fundamental insights into the structure–property relationship, guiding the future design of AIE-active Schiff bases.

Experimental

Materials and methods

All chemicals were purchased from commercial sources and were of analytical grade unless otherwise indicated. Tetrahydrofuran (THF) was purchased from Tianjin Fuyu Chemical Co., Ltd. 1,3-Bis(aminopropyl)tetramethyldisiloxane (MM^{NH_2}) was purchased from Hangzhou Dadi Chemical Co., Ltd. *p*-Hydroxybenzaldehyde and *o*-hydroxybenzaldehyde were obtained from Shanghai Aladdin Bio-Chem Technology Co., Ltd.

For the testing of the synthesized materials, ^{1}H NMR and ^{13}C NMR spectra were recorded on a Bruker AVANCE 300 MHz or AVANCE 400 MHz superconducting NMR spectrometer. UV-Vis absorption spectra were recorded on a Hitachi U3900H spectrophotometer, and FTIR analysis was performed synthesized materials using a Bruker TENSOR-27 FTIR spectrometer. Fluorescence properties were characterized on an F-7000 Fluorescence Spectrophotometer. All experiments were performed at room temperature (25 °C) unless otherwise specified.

Synthesis of PBS

p-Hydroxybenzaldehyde (1.22 g, 0.01 mol) was dissolved in THF (10 mL). A solution of 1,3-bis(3-aminopropyl)-1,1,3,3-tetramethyldisiloxane in THF (10 mL) was then added dropwise to the system at room temperature. The resulting mixture was continuously stirred at 50 °C for 2 h. After the evaporation of the solvent, the crude product was purified, yielding a pale-yellow solid (2.03 g; yield: 89.1%). ^{1}H NMR (400 MHz, CD_3OD, δ, ppm): 9.73 (1H, –OH), 8.14 (1H, –CH=N–), 7.59–7.56 (2H, Ar–H), 6.80–6.78 (2H, Ar–H), 3.52 (2H, =N–CH_2–), 1.74–1.66 (2H, =N–CH_2–**CH_2**–), 0.57–0.53 (2H, –Si–**CH_2**–CH_2), 0.08 (6H, –CH_3). FTIR spectrum (KBr disk, cm^{-1}): 1051 cm^{-1} (Si–O–Si), 1644 cm^{-1} (C=N). ^{13}C NMR: (100 MHz, CD_3OD, δ, ppm; Fig. S1): δ 164.1, 131.8, 126.6, 117.3, 64.0, 25.8, 16.6, 0.45. ESI-HRMS (Fig. S1): *m*/*z* calculated for $[C_{24}H_{37}N_2O_3Si_2]^+$: 457.23, found 457.23 $[M + H]^+$.

Synthesis of OBS

o-Hydroxybenzaldehyde (1.22 g, 0.01 mol) was dissolved in THF (10 mL), after which a solution of 1,3-bis(3-aminopropyl)-1,1,3,3-tetramethyldisiloxane in THF (10 mL) was added dropwise to the system at room temperature. The resulting mixture was stirred continuously at 50 °C for 2 h. After rotary evaporation of the solvent, the crude product was purified, yielding a yellow-green liquid (2.16 g; yield: 94.8%). ^{1}H NMR (400 MHz, $CDCl_3$, δ, ppm; Fig. S3): 13.70 (1H, –OH), 8.31 (1H, –CH=N–), 7.32–7.23 (2H, Ar–H), 6.98–6.87 (2H, Ar–H), 3.57 (2H, =N–CH_2–), 1.72 (2H, =N–CH_2–**CH_2**–), 0.58 (2H, –Si–**CH_2**–CH_2), 0.08 (6H, –CH_3). FTIR spectrum (KBr disk, cm^{-1}): 1054 cm^{-1} (Si–O–Si), 1633 cm^{-1} (C=N). ^{13}C NMR: (100 MHz, CD_3OD, δ, ppm; Fig. S1): δ 166.8, 165.7, 134.2, 133.1, 119.4, 118.9, 118.7. ESI-HRMS (Fig. S1): *m*/*z* calculated for $[C_{24}H_{37}N_2O_3Si_2]^+$: 457.23, found 457.23 $[M + H]^+$.

Results and discussion

Structure characterization

As shown in Fig. 1A, the IR spectra of compound PBS and its reactant MM^{NH_2}, the disappearance of the primary amine bimodal peak near 3300 cm^{-1}, and the absorption of the C=N bond at 1633 cm^{-1} tentatively confirmed the occurrence of the reaction. ^{1}H NMR spectra were recorded on a Bruker 400 (400 MHz) spectrometer without tetramethylsilane as an internal reference and are shown in Fig. 1B. Resonance peaks at 0.08, 0.55, 1.70, and 3.52 ppm—corresponding to –Si–C**H_3**, –Si–C**H_2**–, –Si–CH_2–C**H_2**–, and –C**H_2**–N= , respectively—were clearly observed for PBS. Combined, these results indicated that the Schiff base compound PBS had been successfully synthesized.

Optical properties

UV-vis absorption spectrum. The UV-Vis spectra of PBS in methanol and THF (Fig. 2; OBS in Fig. S3) reveal distinct tautomeric behavior. In methanol, additional peaks at 331 and

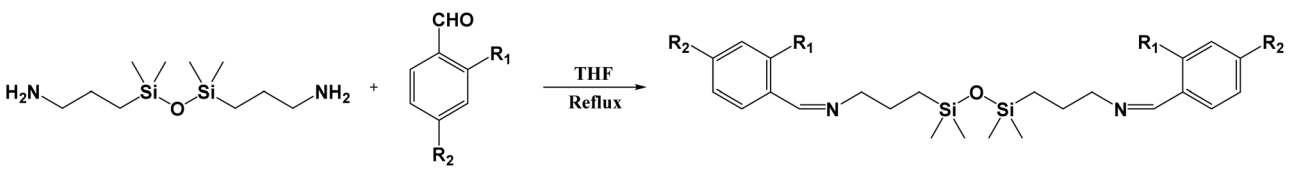

Scheme 1 The synthesis reaction of (a) PBS, R_1 = H, R_2 = OH and (b) OBS, R_1 = OH, R_2 = H.

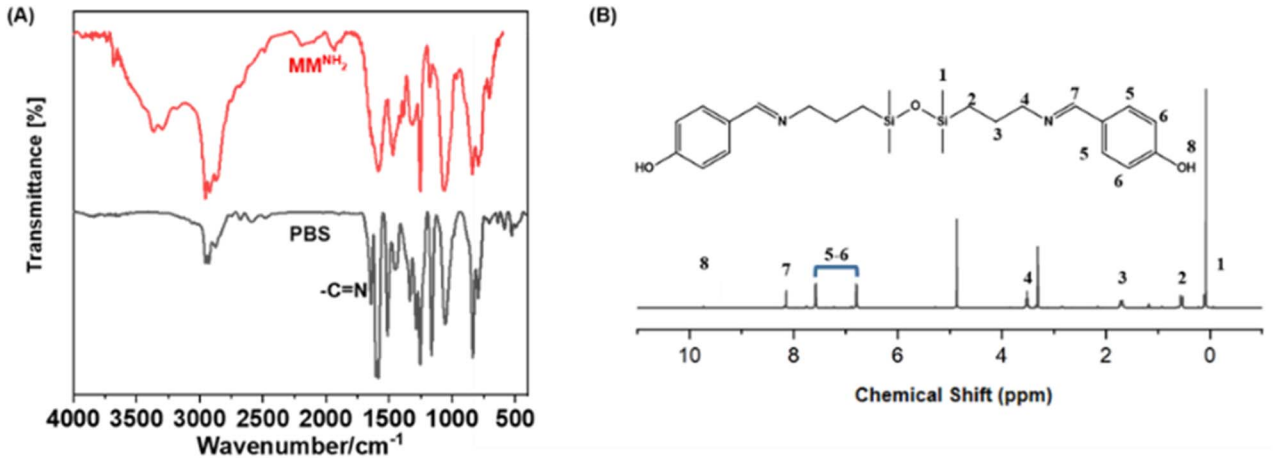

Fig. 1 (A) IR spectrum of PBS and MM^{NH_2} (B) ^1H NMR spectra of PBS.

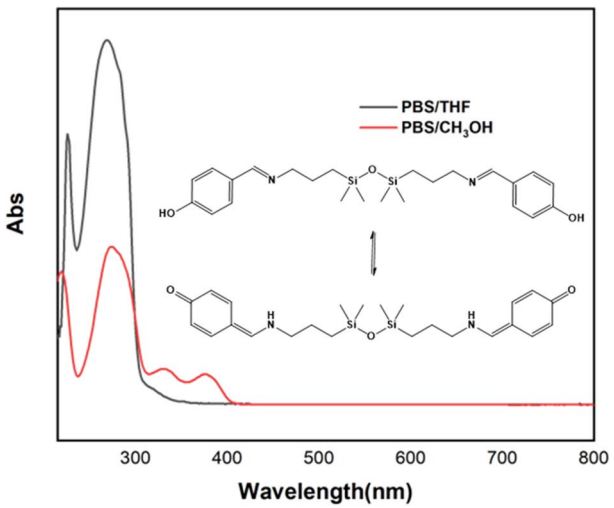

Fig. 2 UV-Vis absorption spectra of PBS in (a) THF, and (b) CH_3OH. Inset: enol-imine and keto-amine forms of PBS.

375 nm appear alongside the aromatic $\pi \rightarrow \pi^*$ transitions at 218 and 253 nm. More notably, the well-resolved bands at ~314 and ~400 nm are assigned to the $n \rightarrow \pi^*$ transitions of the enol-imine and keto-amine tautomers, respectively, confirming C=N formation and coexistence of both forms. The keto-amine band at 400 nm in methanol is stabilized by intermolecular hydrogen bonding with the protic solvent, lowering its energy relative to the enol-imine form.

Although precise tautomer ratios require techniques such as NMR titration or time-resolved spectroscopy, the relative intensity of the ~400 nm band offers a clear qualitative indicator. This band is significantly stronger in PBS than in OBS, particularly in methanol, indicating a higher equilibrium population of the keto-amine tautomer in the *para*-substituted PBS. This trend is attributed to more effective intermolecular hydrogen-bonding stabilization in protic media and aligns with established photophysical trends in analogous Schiff-base systems.[36,37]

Critically, the keto-amine tautomer is recognized as the primary emitting species in such systems,[38–40] governing fluorescence through mechanisms such as excited-state intramolecular proton transfer (ESIPT) and/or intramolecular charge transfer (ICT). Photoexcitation of this form promotes rapid ESIPT or strong ICT, yielding a highly conjugated, planar excited state that emits at longer wavelengths. This mechanism explains the red-shifted emission and pronounced positive solvatochromism observed in PBS, whose higher keto-amine population enhances fluorescence intensity and AIE activity. Conversely, the weaker emission of OBS correlates with its reduced keto-amine absorption, consistent with this framework. Therefore, tautomeric equilibrium not only shapes the absorption profile but also decisively dictates fluorescence outcomes—including emission wavelength, quantum yield, and AIE enhancement—highlighting the central role of tautomerism in the photophysics of these Schiff-base derivatives.

Fluorescence emission spectroscopy. As shown in Fig. 3A, the compound exhibits a maximum emission wavelength at 467 nm. We propose that the conjugation between the –C=N– moiety and the benzene ring extends the electron delocalization range, thereby narrowing the energy gap for electron transitions and enhancing fluorescence. The nitrogen atom of the –C=N– group in the Schiff base synthesized in this work adopts sp^2 hybridization; the presence of a lone pair of electrons makes it a relatively strong electron acceptor with a high propensity for protonation. Additionally, the oxygen atom contains lone-pair electrons that engage in p–π conjugation with the benzene ring. The emission peaks observed at 472 nm and 503 nm are ascribed to the intramolecular interactions between the –OH group (acting as an electron donor) on the benzene ring and the protonated imine group (acting as the acceptor).

To explore how this inherent emissivity translates into aggregate-state behavior, we investigated the concentration-dependent fluorescence of PBS in methanol. As shown in Fig. 3A (focusing on the intensity trend), the emission is negligible in dilute solution but increases sharply with concentration, reaching a maximum at approximately 5×10^{-3} mol L^{-1}.

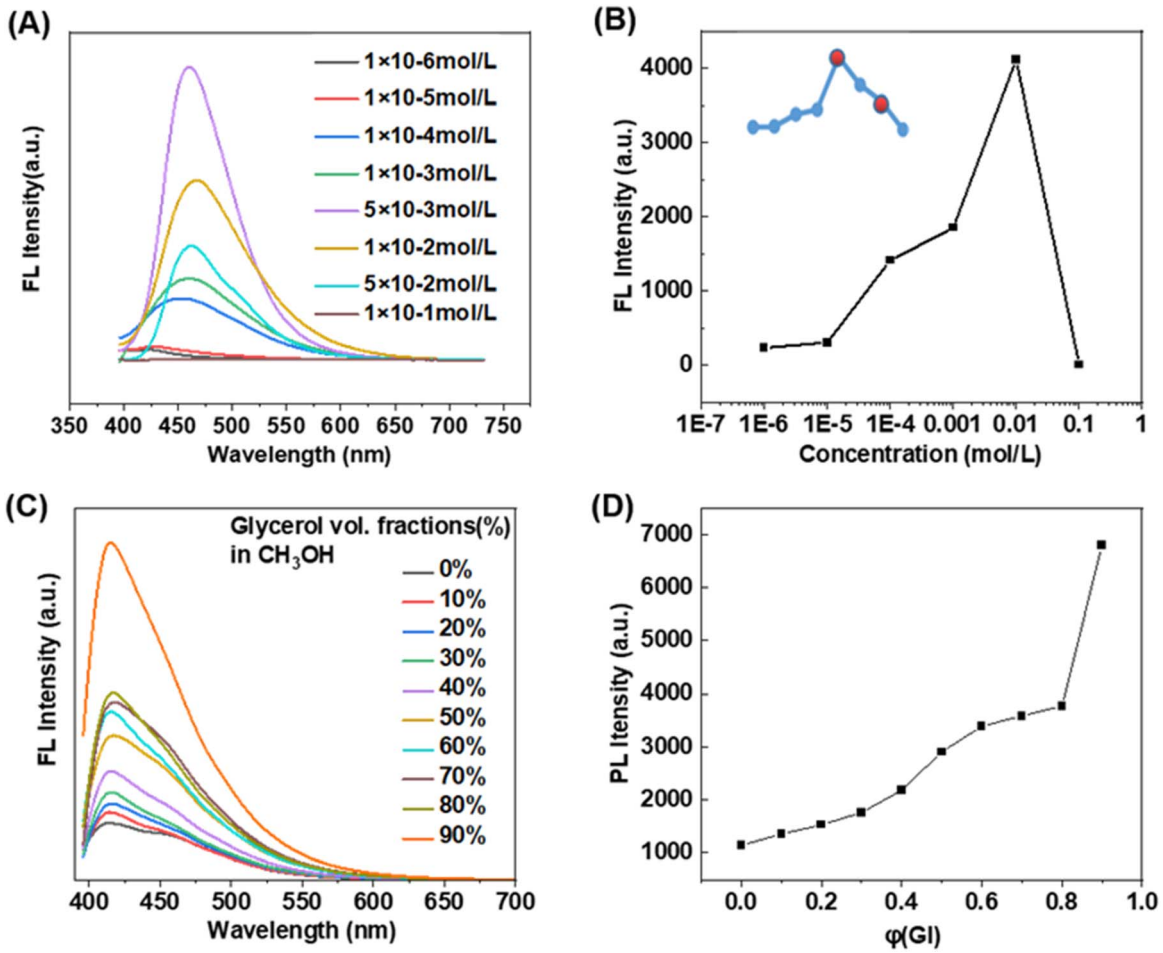

Fig. 3 (A) Fluorescence emission spectra of PBS at varying concentrations, Ex = 376 nm, (B) line graph. Inset: same as the line chart, the red part represents the concentration of 5×10^{-3} mol L^{-1} and 5×10^{-2} mol L^{-1} (from left to right); (C) the fluorescence spectrum of PBS in methanol–glycerol solution, Ex = 376 nm, (D) line graph.

This initial enhancement is characteristic of AIE, attributed to the restriction of intramolecular motion (RIM) in aggregates, which suppresses non-radiative decay. Notably, beyond this optimum concentration, a gradual decrease in intensity is observed (Fig. 3A), likely due to competitive effects such as inner-filtering or the formation of non-emissive excimers at very high concentrations.

To further investigate the influence of solubility on AIE, we altered the solvent environment. Given that the compound displayed lower solubility in hexane than in methanol, we incrementally added hexane to a methanol solution of the compound to examine its AIE response. As demonstrated in Fig. 4A, the fluorescence intensity progressively intensified with increasing hexane content, confirming the AIE characteristics of the material under solvent-induced aggregation. As shown in Fig. 4B, the fluorescence emission spectra of PBS were recorded in a series of solvents with varying polarity. The spectral behavior exhibited a clear dependence on solvent environment.

Systematic comparison of optical properties between PBS and OBS. A systematic comparison of the photophysical properties between the *para*-substituted PBS and *ortho*-substituted OBS reveals distinct structure-dependent behaviors. In UV-Vis absorption spectra recorded in methanol, PBS exhibits two well-resolved bands at 314 nm and 400 nm, corresponding to the n → π* transitions of the enol-imine and keto-amine tautomers, respectively. The significantly higher relative intensity of the ~400 nm band in PBS indicates a greater equilibrium population of the keto-amine tautomer compared to OBS, a qualitative difference attributable to more effective intermolecular hydrogen-bonding stabilization in the *para*-substituted system. In contrast, OBS shows slightly blue-shifted absorption maxima at 310 nm and 395 nm, with a relatively weaker keto-amine band, reflecting its different intramolecular hydrogen-bonding pattern that favors the enol-imine form. This tautomeric distribution has a direct consequence on emission: as the keto-amine form is widely recognized as the primary emitting species due to its capacity for efficient excited-state ICT or proton transfer (ESIPT). Consequently, in the solid state, PBS emits at 467 nm, while OBS displays a red-shifted emission maximum at 480 nm. This shift can be attributed to the stronger intramolecular hydrogen bond in the *ortho*-substituted derivative, which stabilizes a more polar charge-transfer configuration

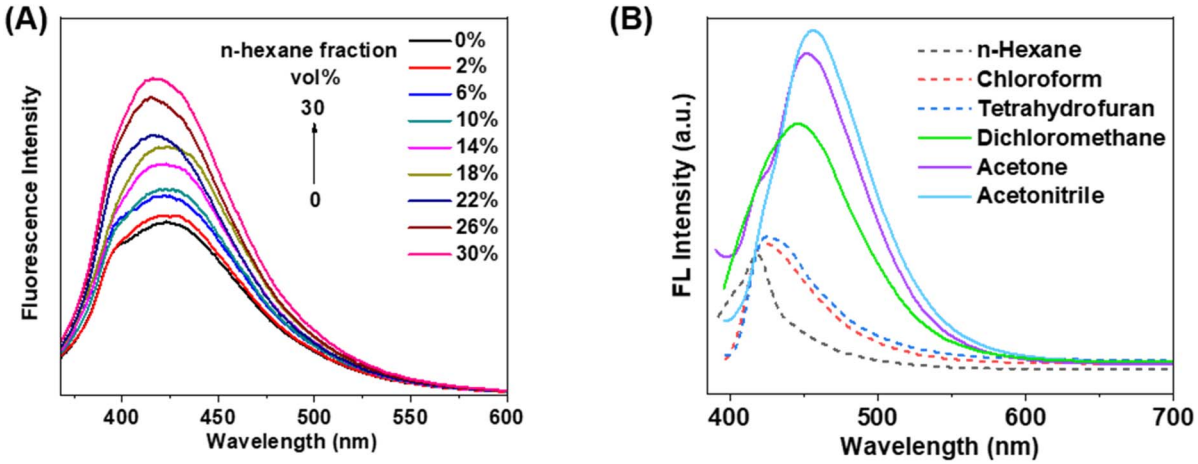

Fig. 4 Fluorescence emission spectra of PBS recorded in different polar solvents. (A) Recorded in *n*-hexane with varying volume fractions (0–30%). (B) Recorded in different polar solvents.

in the excited state. Regarding aggregation-induced emission, PBS exhibits a markedly higher enhancement ratio (~120-fold) compared to OBS (~35-fold), demonstrating that the *para*-substitution geometry more effectively suppresses non-radiative decay pathways in the aggregated state. This correlation is consistent with the higher population of the emissive keto-amine tautomer in PBS, whose radiative process is further favored under restricted molecular motion. This is further corroborated by the stronger overall fluorescence intensity observed for PBS in both solution and solid states. Furthermore, PBS shows a pronounced positive solvatochromism with increasing solvent polarity, accompanied by significant spectral broadening, a hallmark of a strong ICT character originating from its dominant keto-amine excited state. OBS, however, displays a weaker solvent dependence, implying a smaller change in dipole moment upon excitation, which aligns with its lesser contribution from the polar keto-amine tautomer. Collectively, these comparative results underscore that the substitution position critically modulates the tautomeric equilibrium, molecular planarity, hydrogen-bonding network, and charge-transfer efficiency, thereby governing the overall photophysical performance. This structure–property relationship provides a clear guideline for the rational design of AIE-active Schiff-base materials with tailored emission characteristics.

Mechanism of upconversion and AIE

Restriction of intramolecular motions. To further validate the proposed mechanism, we examined the luminescence properties of PBS by systematically increasing solvent viscosity. Fig. 3C displays the fluorescence emission spectra of PBS in methanol/glycerol mixtures with varying volume fractions. The fluorescence intensity gradually increased with increasing glycerol content and exhibited a sharp enhancement when the glycerol fraction (f_w) exceeded 80%, characterized by a strong emission peak at 415 nm. This trend can be attributed to the restricted intramolecular rotation resulting from increased solution viscosity, which suppresses non-radiative relaxation and promotes radiative decay. These results align with our earlier conclusions, further confirming that the Schiff base derivative exhibits typical AIE characteristics.

Additionally, the infcorporation of Si–O–Si units disrupts the formation of a fully planar molecular structure, thereby mitigating the fluorescence quenching caused by π–π stacking interactions. This structural feature likely contributes to the compound's pronounced AIE properties.

Intramolecular charge transfer. As with all third-order nonlinear optical effects, two-photon absorption (2PA) is highly correlated with ICT and the design of non-centrosymmetric dipole molecules. The fluorescence emission spectra of PBS (and OBS, shown in Fig. S4) in different polar solvents are illustrated in Fig. 4B. As the polarity of the solvent increases, the maximum emission wavelength undergoes a redshift, accompanied by a gradual broadening of the peak profile. This solvatochromic effect further confirmed that the compound possesses excited-state characteristics consistent with an ICT state.

The dipole moment of an excited state of a fluorescent molecule is larger than that of the ground state, and an increase in solvent polarity produces a greater stabilizing effect on the excited state than on the ground state. As a result, the fluorescence spectrum shifts to longer wavelengths with increasing solvent polarity. The fluorescence intensity of the compound in more polar solvents, such as THF and acetonitrile, is much greater than that in nonpolar media, such as hexane and triethylamine. This may be attributable to the fact that the energy difference (ΔE) required for the $\pi \rightarrow \pi^*$ transition is reduced in polar solvents. The increased transition probability results in a redshift in both the UV absorption and fluorescence emission wavelengths, alongside an enhancement in emission intensity.

Density functional theory

To gain further insight into the influence of the molecular structure on the ICT characteristics, the frontier molecular orbitals—specifically, the highest occupied molecular orbital

(HOMO) and the lowest unoccupied molecular orbital (LUMO)—were calculated. All electronic structure simulations were performed with Gaussian 16 software. The CAM-B3LYP functional was adopted for all calculations. For geometry optimization and frequency calculations, the 6-311G(d) basis set34 was used, and the optimal geometry for each compound was determined.

The molecular structure, ground-state geometry optimization structure, and frontier orbital electron cloud distribution of compound PBS are shown in Fig. S7 (Fig. S6 for OBS). The geometric optimization results indicate that the torsion angles (C=N and benzene ring planes) in both the ground-state and the excited state are close to 0°. This relatively planar geometric configuration is conducive to charge transfer, which provides favorable conditions for ICT.

The electron clouds on the HOMO orbitals of the optimized ground-state geometry are almost predominantly distributed throughout the conjugated part (left side), while the electron clouds on the HOMO orbitals of the optimized excited-state geometry are mostly localized around C=N, which supports the presence of a strong ICT. Simultaneously, sufficient orbital overlap ensures a reasonable radiative transition rate, while the change in the electron cloud distribution distinguishes this excited state from a localized excited state.

A more rigorous explanation for the fluorescence behavior of the AIEgens in solution involves π-twisting and distortion in the excited state, which may lead to a minimum energy conical intersection and subsequent non-radiative decay. The geometrical optimization results clearly indicate that a more planar geometric configuration of the fluorescent moiety favors enhanced emission even in solution. Additionally, the distorted conformation of the Si–O–Si fragment expands the intermolecular distance, thus significantly suppressing intermolecular π–π interactions and further ensuring fluorescence emission in the aggregated state.

Conclusions

In summary, two novel siloxane-containing Schiff base compounds were synthesized, and their fluorescence properties were evaluated at different concentrations. The results showed that conjugation of the –C=N bond with the benzene ring and the siloxane helical structure imparts unique fluorescent properties, offering new insights for enhancing the AIE characteristics of such materials. The strong AIE luminescence of compound PBS is primarily attributed to the RIM mechanism. Furthermore, the presence of ICT within the molecule was corroborated by both DFT calculations and fluorescence assays in various solvents. Such an AIE-active compound overcomes the limitation of most organic luminescent materials, which typically do not emit light in aggregated forms, such as thin films, making it highly promising for diverse applications. These include the development of organic electroluminescent devices, chemical sensing, and, in particular, advanced bioimaging platforms.

Author contributions

Yuling Li: conceptualization, resources, investigation, writing – original draft. Depeng Ma: conceptualization, data curation, validation, writing – original draft. Fanzhen Kong: data curation, validation, writing – original draft, formal analysis. Yuanrong Wang: funding acquisition, supervision, writing – review & editing. Lianfeng Wu: conceptualization, funding acquisition, supervision, validation, writing – review & editing. Zhihui Yang: conceptualization, funding acquisition, supervision, visualization, writing – review & editing. Haifeng Lu: conceptualization, funding acquisition, supervision, validation, writing – review & editing.

Conflicts of interest

The authors declare no conflict of interest.

Data availability

The data supporting the findings of this study are available in the supplementary information (SI), which includes characterization data (NMR, HRMS, and IR spectra), photophysical properties (UV-vis absorption, fluorescence emission in various solvents, and concentration-dependent emission), and theoretical calculations (ground- and excited-state optimized geometries and frontier molecular orbital electron cloud distributions) for PBS and OBS. See DOI: https://doi.org/10.1039/d5ra10030e.

Acknowledgements

We thank the National Key R&D Program of China (2022YFF1400300) for supporting our work. This project was supported by the open project funding of the State Key Laboratory of Coatings for Advanced Equipment. The authors acknowledge the assistance of Shandong University Structural Constituent and Physical Property Research Facilities/SDU SC&PP Research Facilities/SDU SCPPRF.

References

1 A. L. Berhanu, I. Malik, A. K. Aulakh, J. SinghKumar and V. K. Ki-Hyun, *TrAC, Trends Anal. Chem.*, 2019, **116**, 74–91.
2 M. T. Kaczmarek, M. Zabiszak, M. Nowak and R. Jastrzab, *Coord. Chem. Rev.*, 2018, **370**, 42–54.
3 L. Chen, T. Fu, H. B. Zhao, D. M. Guo, X. L. Wang and Y. Z. Wang, *Chem. Eng. J.*, 2018, **336**, 622–632.
4 G. Li, Q. Lin, L. Sun, C. Feng, P. Zhang, B. Yu, Y. Chen, Y. Wen, H. Wang and L. Ji, *Biomaterials*, 2015, **53**, 285–295.
5 A. K. Singh and L. K. Kumawat, *Sens. Actuators, B*, 2014, **195**, 98–108.
6 J. Jayabharathi, V. Thanikachalam, K. Jayamoorthy and M. V. Perumal, *Spectrochim. Acta, Part A*, 2011, **79**, 6–16.
7 T. Jing and L. Yan, *Talanta*, 2017, **170**, 185–192.
8 D. Li, X. Liang, F. Zhang, J. Li, Z. Zhang, S. Wang, Z. Li, Y. Xing and K. Guo, *J. Mater. Chem. C*, 2022, **10**, 11016–11026.

9 J. Mei, Y. Hong, J. W. Y. Lam, A. Qin, Y. Tang and B. Z. Tang, *Adv. Mater.*, 2014, **26**, 5429–5479.
10 S. Yang, Y. Yuan, X. Wang, Z. Hu and D. Guo, *J. Lumin.*, 2022, **242**, 118560.
11 S. Huang, J. Ding, A. Bi, K. Yu and W. Zeng, *Adv. Opt. Mater.*, 2021, **9**, 2170086.
12 L. Wu, N. Liang, X. Yang, W. Pan, Y. Wang and L. Zhao, *J. Photochem. Photobiol., A*, 2021, **420**, 113506.
13 Y. Zhang, P. Zhuo, H. Yin, Y. Fan, J. Zhang, X. Liu and Z. Chen, *ACS Appl. Mater. Interfaces*, 2019, **11**, 24395–24403.
14 C. Zhou, W. Xu, P. Zhang, M. Jiang, Y. Chen, R. T. K. Kwok, M. M. S. Lee, G. Shan, R. Qi and X. Zhou, *Adv. Funct. Mater.*, 2019, **29**, 1805986.
15 H. Dong, S. R. Du, X. Y. Zheng, G. M. Lyu, L. D. Sun, L. D. Li, P. Z. Zhang, C. Zhang and C. H. Yan, *Chem. Rev.*, 2015, **115**, 10725–10815.
16 B. Zhou, Q. Li, L. Yan and Q. Zhang, *J. Rare Earths*, 2020, **38**, 474–482.
17 L. Cheng, C. Wang and Z. Liu, *Nanoscale*, 2012, **5**, 23–37.
18 G. Chen, H. Qiu, P. N. Prasad and X. Chen, *Chem. Rev.*, 2014, **114**, 5161–5214.
19 Y. Sun, W. Feng, P. Yang, C. Huang and F. Li, *Chem. Soc. Rev.*, 2015, **44**, 1299–1301.
20 D. Yin, C. Wang, J. Ouyang, X. Y. Zhang and M. Wu, *ACS Appl. Mater. Interfaces*, 2014, **6**, 18480–18488.
21 P. Duan, N. Yanai, Y. Kurashige and N. Kimizuka, *Angew. Chem.*, 2015, **127**, 7654–7659.
22 S. Hisamitsu, N. Yanai and N. Kimizuka, *Angew. Chem.*, 2015, **127**, 11712–11716.
23 Y. Wang, Y. Li, Z. Zhang, L. Wang, D. Wang and B. Z. Tang, *Adv. Mater.*, 2021, **33**, 2103748.
24 Z. Qu, P. Duan, J. Zhou, Y. Wang and M. Liu, *Nanoscale*, 2018, **10**, 985–991.
25 Y. Wang, N. Niu, Y. Huang, S. Song, H. Tan, L. Wang, D. Wang and B. Z. Tang, *Small Methods*, 2022, **6**, 2200393.
26 J. H. Yang, L. Du, J. X. Guo, L. Zhang, S. G. Wang and X. H. Wang, *Int. J. Biol. Macromol.*, 2025, **308**(4), 142572, DOI: 10.1016/j.ijbiomac.2025.142572.
27 L. P. Zong, X. J. Li, D. R. Zhu, X. W. Guo, J. Chauvin, S. L. Zhang, G. Y. Zhang, K. Krukiewicz, S. Cosnier, X. J. Zhang and D. Shan, *ACS Sens.*, 2025, **10**(9), 7134–7143, DOI: 10.1021/acssensors.5c02452.
28 H. Jafari, E. Ameri, M. Hassan Vakili and A. Berisha, *Electrochem. Commun.*, 2024, **159**, 107653, DOI: 10.1016/j.elecom.2023.107653.
29 I. Chaturvedi, S. Vyas and R. Mishra, *Dyes Pigm.*, 2025, **239**, 112748, DOI: 10.1016/j.dyepig.2025.112748.
30 D. A. Chen, J. Li, Z. H. Li, T. Deng and J. S. Li, *Talanta*, 2025, **295**, 128332, DOI: 10.1016/j.talanta.2025.128332.
31 R. Arabahmadi and S. Kamali, *J. Water Process Eng.*, 2025, **76**, 108230, DOI: 10.1016/j.jwpe.2025.108230.
32 S. Yang, J. Zhang, G. Y. Liu, R. Wang and X. Q. Zhang, *Compos. Commun.*, 2025, **54**, 102257, DOI: 10.1016/j.coco.2025.102257.
33 H. Liu, D. Ren, H. Geng, Y. Tian, M. Li, N. Wang, S. Yuan, J. Hao and J. Cui, *Adv. Healthcare Mater.*, 2025, **14**, 2403865, DOI: 10.1002/adhm.202403865.
34 L. Wang and Y. Chen, *Mater. Horiz.*, 2025, **12**, 2709–2721, DOI: 10.1039/d4mh01546k.
35 V. Sharma, S. Dutta, D. Sahu, A. Pandey, D. Kumar, J. Mayee Bag and G. Kumar Patra, *Inorg. Chem. Commun.*, 2025, **181**(1), 115110, DOI: 10.1016/j.inoche.2025.115110.
36 N. M. D. Brown and D. C. Nonhebel, *Tetrahedron*, 1968, **24**(16), 5655–5664, DOI: 10.1016/0040-4020(68)88164-5.
37 İ. Sıdır, Y. Gülseven Sıdır, H. Berber, M. L. Ramos, L. L. G. Justino and R. Fausto, *Molecules*, 2025, **30**, 745, DOI: 10.3390/molecules3003074.
38 I. Sıdır, Y. G. Sıdır, H. Berber and R. Fausto, *J. Mol. Struct.*, 2023, **1292**, 136191.
39 X. Y. Cheng, T. S. Zhang, Z. L. Li and K. Zhao, *J. Phys. Chem. B*, 2025, **129**(24), 6061–6068.
40 T. Jiang, J. H. Lu, C. Huang, D. M. Chen and B. X. Zhu, *Dyes Pigm.*, 2024, **223**, 111972.